Journal of Materials Chemistry C

ROYAL SOCIETY OF CHEMISTRY

PAPER

View Article Online
View Journal | View Issue

Cite this: J. Mater. Chem. C, 2026, 14, 232

The role of a [2.2]paracyclophane moiety in piezofluorochromism of crystalline organoboron complexes

Shun Irii,[a] Takuya Ogaki,[ab]* Shun Yamamoto,[a] Hana Miyashita,[c] Kazutaka Nobori,[c] Hiroki Iida,[c] Yoshiki Ozawa,[c] Masaaki Abe,[c]* Hiroyasu Sato,[d] Yasunori Matsui[ab] and Hiroshi Ikeda[ab]*

Received 25th August 2025,
Accepted 17th October 2025

DOI: 10.1039/d5tc03195h

rsc.li/materials-c

Fluorescence (FL) properties of crystals of [2.2]paracyclophane-containing organoboron complexes (***p*CP-H** and ***p*CP-iPr**) were investigated under high pressure using a diamond anvil cell to evaluate the effects of intramolecular π–π interactions in the [2.2]paracyclophane moiety on piezofluorochromism (PFC). Crystals of both ***p*CP-H** and ***p*CP-iPr** were found to display remarkable PFC with redshifts of more than 100 nm under high pressures up to *ca.* 8 GPa. However, the pressure-sensitivities of FL of ***p*CP-H** and ***p*CP-iPr** crystals differed. The results of X-ray crystallography studies under ambient and high pressure revealed that PFC of the ***p*CP-H** crystal mainly originates from intermolecular π–π interactions taking place in a π-stacked dimer. Density functional theory calculations also showed that intermolecular orbital interactions in the π-stacked dimer play an important role in the PFC of ***p*CP-H**. In contrast, it was found that ***p*CP-iPr** does not form a π-stacked dimer in the crystal state. Therefore, PFC of the ***p*CP-iPr** crystal is mainly controlled by intramolecular π–π interactions in the [2.2]paracyclophane moiety, making it less sensitive than ***p*CP-H** to pressure changes.

Introduction

Crystals of many aromatic compounds undergo reversible changes in their fluorescence color upon application of an external stimulus, such as grinding and exposure to organic solvent vapor.[1,2] The fluorescence changes of these crystals are a consequence of changes that take place in their flexible crystal structures. Piezofluorochromism (PFC) is a term used to characterize changes in the fluorescence (FL) color of crystals that occur reversibly in response to isotropic pressure changes.[3–5] Since the late 1970s, many studies have shown that crystals of aromatic molecules[3–9] display PFC in association with drastic FL color changes taking place under extremely high, GPa range pressures applied by using a diamond anvil cell (DAC).[10–14] Because these FL color changes are reversed simply by removing the applied pressure, PFC has attracted the attention of not only physical organic chemists, having interests in the structural/electronic foundation of the process, but also scientists developing new types of pressure sensors. PFC of crystals of organic molecules can be roughly classified into two classes depending upon whether it is promoted by changes in intermolecular or intramolecular interactions. In the former route, application of high, GPa range pressure leads to a decrease in the distance between molecules in the crystal and a subsequent increase in intermolecular π–π interactions. Typically, reducing the distance between π-planes of molecules in a crystal leads to destabilization of the ground state, but it promotes stabilization of the photoexcited state *via* excimer formation that is accompanied by redshifted excimer FL.[15–24] In the intramolecular mechanism for PFC, high pressure induces an increase in π-conjugation in a molecule in the crystal as a consequence of a decrease in rotational freedom. For example, in aromatic molecules containing donor and acceptor moieties and that have intramolecular charge transfer (ICT) photoexcited states, applying high pressure can reduce the dihedral angle between the donor and acceptor moieties, resulting in stabilization of the photoexcited ICT state owing to more extensive intramolecular π-conjugation.[20,25] However, the operational efficiencies of the two mechanisms depend not only on the structure of the molecule but also molecular packing in the crystal. This feature makes it difficult to control PFC in organic molecular crystals.

[a] *Department of Applied Chemistry, Graduate School of Engineering, Osaka Metropolitan University, 1-1 Gakuen-cho, Naka-ku, Sakai, Osaka 599-8531, Japan. E-mail: hiroshi_ikeda@omu.ac.jp, takuya_ogaki@omu.ac.jp*
[b] *The Research Institute for Molecular Electronic Devices (RIMED), Osaka Metropolitan University, 1-1 Gakuen-cho, Naka-ku, Sakai, Osaka 599-8531, Japan*
[c] *Department of Material Science, Graduate School of Science, University of Hyogo, 3-2-1 Kouto, Kamigori, Ako, Hyogo 678-1297, Japan. E-mail: mabe@sci.u-hyogo.ac.jp*
[d] *Rigaku Corporation, 3-9-12 Matsubara-cho, Akishima, Tokyo 196-8666, Japan*

The aim of this study was to gain information about the pressure-sensitivity of an intramolecular π–π interaction.[26] [2.2]Paracyclophane is a molecule composed of two benzene rings possessing an intramolecular π-stacked dimer fixed by the presence of two ethylene linkers at *para*-positions.[27–29] Strong intramolecular π–π interactions in these substances lead to a unique array of electronic and optical properties.[30–33] Based on the expectation that this type of intramolecular π–π interaction should enable [2.2]paracyclophane to display pressure-sensitivity and consequent PFC[34] in a crystal structure independent manner, in an earlier study,[35] we evaluated the PFC properties of a crystal of the [2.2]paracyclophane-containing organoboron complex with a *para-tert*-butylphenyl substituent (***p*CP-*t*Bu**, Chart 1). We anticipated that this substance would display pressure-sensitive fluorescence[36–38] owing solely to changes in intramolecular π–π interactions in the [2.2]paracyclophane moiety.[34] Specifically, we reasoned that the *p-tert*-butyl group on the phenyl ring in ***p*CP-*t*Bu** would significantly reduce PFC caused by intermolecular π–π interactions. Indeed, the ***p*CP-*t*Bu** crystal did exhibit remarkable PFC corresponding to a more than 150 nm shift in its emission maximum under high pressure applied in a DAC. However, in contrast to our expectation, the results of X-ray crystallographic analyses and theoretical calculations showed that PFC of the ***p*CP-*t*Bu** crystal is caused by changes in intermolecular π–π interactions taking place in a π-stacked dimer formed in the crystal. Although X-ray crystallography data showed that the size of the [2.2]paracyclophane moiety in the ***p*CP-*t*Bu** crystal decreases significantly under high pressure, it remained unclear how the intramolecular π–π interactions influence the PFC properties.

The apparent ambiguity in the results observed from our previous study stimulated an investigation to assess in detail the role that the [2.2]paracyclophane moiety in these substances plays in determining the intensity and mechanistic nature of PFC. For this purpose, we prepared the parent ***p*CP-H**[39,40] (Chart 1) and its isopropyl derivative ***p*CP-iPr** and investigated the pressure-sensitivity of their FL properties in the crystalline state. As described below, the results of this study demonstrated that while both complexes display PFC, the mechanisms responsible for these processes differ. Specifically, the results indicate that ***p*CP-H** crystals exhibit "pressure-sensitive" PFC owing mainly to changes in intermolecular π–π interactions occurring in π-stacked dimers, whereas ***p*CP-iPr** crystals display "pressure-insensitive" PFC owing to intramolecular π–π interactions in the [2.2]paracyclophane moiety.

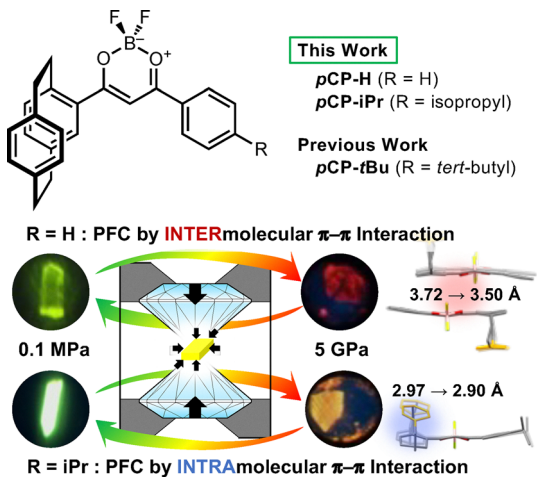

Chart 1 Graphical description of key features of this study. (top) Molecular structures of ***p*CP-H**, ***p*CP-iPr**, and ***p*CP-*t*Bu**. (bottom) An illustration of PFC of the ***p*CP-H** and ***p*CP-iPr** crystals in a diamond anvil cell.

Results and discussion

Racemic mixtures of ***p*CP-H** and ***p*CP-iPr** were synthesized using previously described[35,39] three step sequences starting with 4-acetyl[2.2]paracyclophane (**1**) (Scheme 1). Detailed descriptions of the methods are given in the Experimental section.

Photophysical properties of *p*CP-H and *p*CP-iPr in CH_2Cl_2 and in crystalline states at ambient pressure. Photophysical properties of ***p*CP-H** in CH_2Cl_2 (1×10^{-5} M) are given in Table 1. As has been reported earlier,[39] the absorption spectrum of ***p*CP-H** in CH_2Cl_2 consists of a broad band with a maximum ($\lambda_{AB,MAX}$) at 393 nm. Upon photoexcitation at 393 nm, a solution of ***p*CP-H** in CH_2Cl_2 displays yellow FL with a maximum ($\lambda_{FL,MAX}$) at 557 nm and a quantum yield (Φ_{FL}) of 0.05 (Fig. 1a). The FL decay profile of ***p*CP-H** in CH_2Cl_2, fitted using a single exponential, showed a FL lifetime (τ_{FL}) of 10.4 ns.

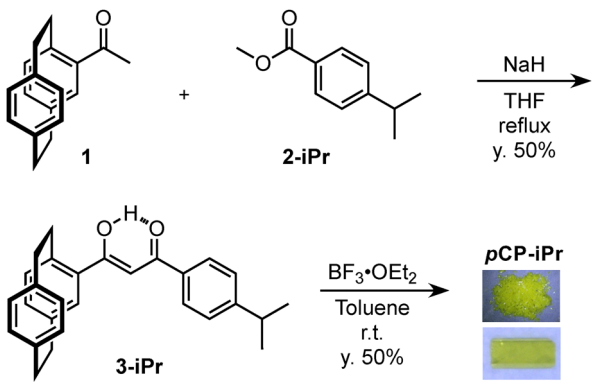

Scheme 1 Synthesis of ***p*CP-iPr**. The insets are photographs of ***p*CP-iPr** under room light.

Table 1 Photophysical properties of ***p*CP-H** and ***p*CP-iPr** in CH_2Cl_2 (1×10^{-5} M) and crystalline states

Substances	State	$\lambda_{AB,MAX}$ [nm]	$\lambda_{FL,MAX}$[a] [nm]	Φ_{FL}[a]	τ_{FL}[bc] [ns]
***p*CP-H**	In CH_2Cl_2	393	557	0.05	10.4 (100%)
	In crystal	—	537	0.11	5.9 (24%)
					14.6 (76%)
***p*CP-iPr**	In CH_2Cl_2	398	546	0.05	10.8 (100%)
	In crystal	—	538	0.10	5.0 (30%)
					14.5 (70%)

[a] Excited at $\lambda_{AB,MAX}$ in CH_2Cl_2. [b] Excited at 371 nm. Detected at each $\lambda_{FL,MAX}$. [c] The percentage in the parentheses shows the ratio of each τ_{FL}.

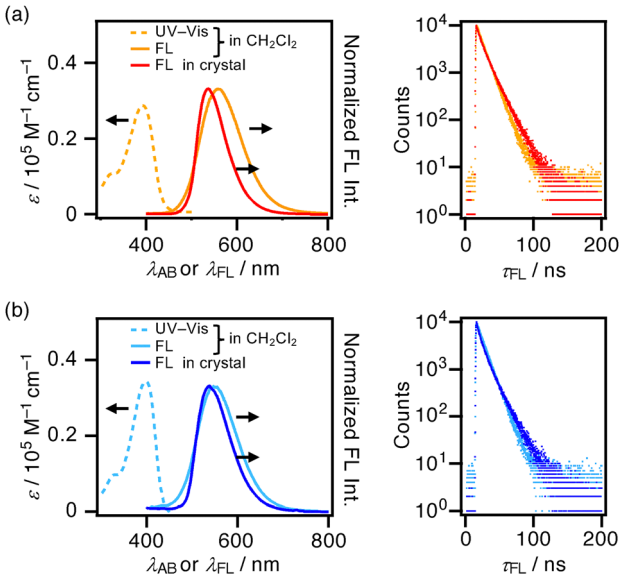

Fig. 1 UV-vis absorption and FL spectra (left), and FL decay curves (right) of (a) ***p*CP-H** and (b) ***p*CP-iPr** in CH_2Cl_2 (1×10^{-5} M) and in crystalline states. FL spectra in CH_2Cl_2 and crystalline states were obtained using excitation at absorption maxima. FL decay curves were obtained by excitation at 371 nm.

***p*CP-iPr** in CH_2Cl_2 has the same photophysical properties as does ***p*CP-H** (Fig. 1b and Table 1), showing that little difference exists between the electronic states of ***p*CP-H** and ***p*CP-iPr**.

Under UV light, ***p*CP-H** and ***p*CP-iPr** crystals exhibit green FL emission with respective $\lambda_{FL,MAX}$ values of 537 and 538 nm (Fig. 1, Table 1). Unlike the method used to analyse solution state data, FL decay profiles of the crystals were fitted using biexponential curves, which provide τ_{FL} values of 5.9 (24%) and 14.6 ns (76%) for the ***p*CP-H** crystal and 5.0 (30%) and 14.5 ns (70%) for the ***p*CP-iPr** crystal. Therefore, the findings indicate that ***p*CP-H** and ***p*CP-iPr** crystals have similar lowest excited singlet states and electronic structures under ambient pressure.

FL properties of *p*CP-H and *p*CP-iPr crystals under high pressure. FL measurements under high pressure, performed using a DAC, showed that both the ***p*CP-H** and ***p*CP-iPr** crystals display PFC. Details of the measurement conditions are given in the Experimental section. Upon stepwise compression from 0.1 MPa to 5.6 GPa, the $\lambda_{FL,MAX}$ of the ***p*CP-H** crystal undergoes a remarkable redshift from 520 to 658 nm, along with a corresponding FL color change from green to dark red and a decrease in FL intensity (Fig. 2a). In the high pressure region above 5.6 GPa, changes in the FL intensity and $\lambda_{FL,MAX}$ become less pronounced, and at 8.1 GPa, the $\lambda_{FL,MAX}$ reaches a plateau at 664 nm. When the applied pressure is gradually reduced, the $\lambda_{FL,MAX}$ returns from 664 nm at 8.1 GPa to 520 nm at 0.1 MPa. On this occasion, the ***p*CP-H** crystal color changed from yellow to red under high pressure, suggesting that the electronic structure of the ground state also changes (Fig. S5a).

In an earlier study,[35] we observed that the energy at the $\lambda_{FL,MAX}$ ($E_{FL,MAX} = hc/\lambda_{FL,MAX}$) of the ***p*CP-*t*Bu** crystal changes in multiple stages as the pressure is increased (compression) and

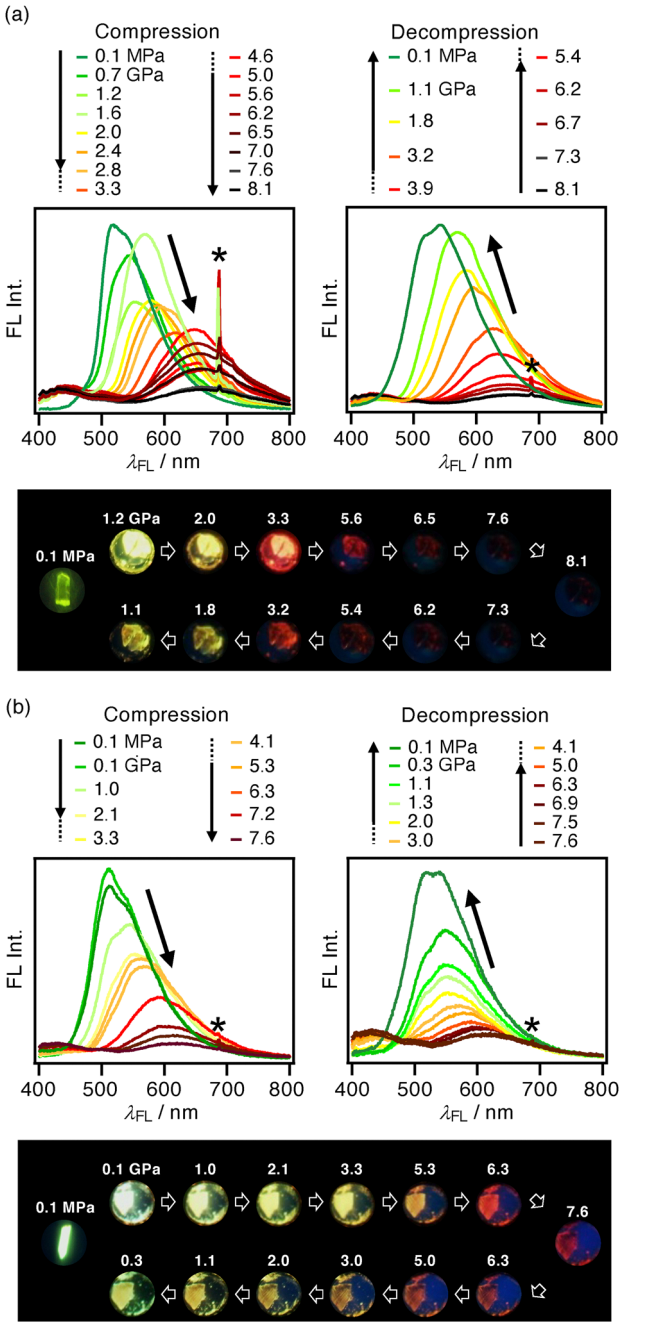

Fig. 2 (top) FL spectra and (bottom) photographs of the (a) ***p*CP-H** and (b) ***p*CP-iPr** crystals under various pressures (λ_{EX} = 365 nm). The photographs at 0.1 MPa and under high pressure were taken using different crystals. FL spectra were recorded a few minutes after the compression or decompression procedure was performed. Crystal sizes are *ca.* 0.2 × 0.2 × 0.1 mm^3. The asterisk stands for FL of a ruby chip.

decreased (decompression) and that the compression and decompression processes have different profiles. Specifically, the ***p*CP-*t*Bu** crystal exhibits PFC with hysteresis. A plot of $E_{FL,MAX}$ for crystalline ***p*CP-H** *vs.* pressure (P), given in Fig. 3, shows that the $E_{FL,MAX}$ of the ***p*CP-H** crystal arises and disappears in three stages (Stages i–iii) and that the stepwise changes in $E_{FL,MAX}$ are also found at the same location during

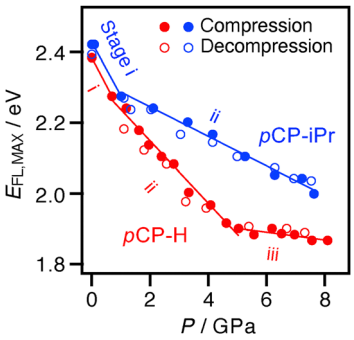

Fig. 3 Plots of energies at FL maxima ($E_{FL,MAX}$) *vs.* applied pressure (P) for the ***p*CP-H** (red) and ***p*CP-iPr** (blue) crystals. The fitted lines are drawn using the points in the compression processes.

Table 2 Slopes of the $E_{FL,MAX}$ *vs.* P plots of the ***p*CP-H** and ***p*CP-iPr** crystals during the compression process

	Slope [eV GPa^{-1}]		
Crystal	Stage i	Stage ii	Stage iii
***p*CP-H**	-15.6×10^{-2}	-8.85×10^{-2}	-1.09×10^{-2}
***p*CP-iPr**	-15.0×10^{-2}	-4.18×10^{-2}	—

both the compression and decompression stages. This observation suggests that the PFC of the ***p*CP-H** crystal is different from that of the ***p*CP-*t*Bu** crystal in that it is microscopically reversible. In stage i (0.1 MPa–0.7 GPa) and stage ii (0.7–5.0 GPa), the $E_{FL,MAX}$ of the ***p*CP-H** crystal decreases steeply with respective slopes of -15.6×10^{-2} and -8.85×10^{-2} eV GPa^{-1} (Table 2). In contrast, the slope of the plot in stage iii (5.0–8.1 GPa) of -1.09×10^{-2} eV GPa^{-1} is smaller by about one tenth of that in stage ii. One possible reason for the significant flattening in stage iii is likely because the intermolecular distance reaches its shortest limit at *ca.* 5 GPa. An alternative explanation is a phase transition, but it is currently impossible to determine whether this is the case.

In the initial phase of the compression (0.1 MPa–1.0 GPa) of the ***p*CP-iPr** crystal, the intensity at the $\lambda_{FL,MAX}$ undergoes only a small decrease (Fig. 2b). At higher pressures, the $\lambda_{FL,MAX}$ exhibits a red shift from 518 nm at 0.1 GPa to 620 nm at 7.6 GPa and a corresponding FL color change from green to red with changes in the ***p*CP-iPr** crystal color from yellow to red (Fig. 2b and Fig. S5b). Moreover, during decompression from 7.6 GPa to 0.1 MPa, the FL of the ***p*CP-iPr** crystal returns to almost the original state at 0.1 MPa. This finding reveals that the ***p*CP-iPr** crystal also displays PFC. The pressure-induced shift of the $E_{FL,MAX}$ of the ***p*CP-iPr** crystal takes place in two stages and is microscopically reversible (Fig. 3). In stage i (0.1 MPa–1.0 GPa), the slope of the plot of $E_{FL,MAX}$ *vs.* P is -15.0×10^{-2} eV GPa^{-1}, a value that is almost the same as that for stage i compression of the ***p*CP-H** crystal. However, the slope of the plot for the ***p*CP-iPr** crystal in stage ii is -4.18×10^{-2} eV GPa^{-1}, which is about half of that of compression of the ***p*CP-H** crystal in stage ii. Therefore, the ***p*CP-H** crystal displays "pressure-sensitive" PFC, while ***p*CP-iPr** exhibits only a "pressure-insensitive" PFC.

It is also noteworthy that the $E_{FL,MAX}$ change of the ***p*CP-iPr** crystal is linear in the 1–8 GPa region. Although the measurements above 8 GPa are not possible owing to equipment limitations, we anticipate that the ***p*CP-iPr** crystal would display PFC at even higher pressures.

Crystal structures of *p*CP-H and *p*CP-iPr at ambient and high pressures. To elucidate the mechanism which induces the difference in the pressure-sensitivity of the FL in stage ii, we next assessed the structural changes that occur in ***p*CP-H** and ***p*CP-iPr** crystals when exposed to a high pressure of 3.1 GPa. X-ray crystallographic analysis at 0.1 MPa revealed that the ***p*CP-H** crystal is racemic and belongs to a trigonal system with the $R\bar{3}$ space group. The crystal is composed of a π-stacked dimer of the S_p- and R_p-enantiomers of ***p*CP-H**, and back sides of the π-planes of the benzene and dihydrodioxaborinine rings in each enantiomer are engaged in strong intermolecular π–π interactions (Fig. 4a).

A comparison of the X-ray crystallographic data of the ***p*CP-H** crystal at different pressures enables an analysis of pressure-induced structural changes that lead to the PFC. While proceeding from 0.1 MPa to 3.1 GPa, the unit cell of the ***p*CP-H** crystal is compressed isotropically to 91% of its original volume, a phenomenon that is associated with a reduction in the distance between the two molecules in the π-stacked dimer (Fig. S7). However, the crystal system and the space group are not changed by the pressure increase, indicating that the ***p*CP-H** crystal does not undergo a phase transition in the range of 0.1 MPa to 3.1 GPa. Although the ***p*CP-H** crystal is compressed under high pressure, shrinkage of the [2.2]paracyclophane moiety does not take place. This conclusion comes from the observation that the intramolecular π-stacked distance (D_{INTRA}) between centroids of two benzene rings in the [2.2]paracyclophane moieties is 2.96 Å at both 0.1 MPa and 3.1 GPa (Fig. 4a). Non-covalent interaction (NCI) plots, which enable visualization of intra- and intermolecular interactions,[41–43] also show that no remarkable changes occur in proceeding from 0.1 MPa to 3.1 GPa (Fig. 4c). These observations suggest that the intramolecular π–π interaction of the [2.2]paracyclophane moiety in the ***p*CP-H** crystal is not pressure-sensitive and, therefore, that this interaction is not responsible for the observed PFC. The intermolecular π-stacked distance (D_{INTER}) decreased from 3.72 Å at 0.1 MPa to 3.50 Å at 3.1 GPa. The changes in the D_{INTER} was subjected to Hirshfeld surface analysis,[44–46] which clearly shows that the enhancement of intermolecular π–π interactions at high pressure (Fig. 4c) is the main reason for the PFC of the ***p*CP-H** crystal.

An analogous X-ray crystallographic analysis of the ***p*CP-iPr** crystal gave results that are contrastingly different from those obtained from studies with the ***p*CP-H** crystal. First, the ***p*CP-iPr** crystal at 0.1 MPa belongs to the orthorhombic crystal system with the $P2_12_12_1$ space group. The ***p*CP-iPr** crystal is homochiral owing to spontaneous resolution and an S_p crystal was subjected to the analysis (Fig. 4b). Because of this feature, the ***p*CP-iPr** crystal does not form a π-stacked dimer with a strong intermolecular orbital overlap like that present in the ***p*CP-H** crystal. Molecules of ***p*CP-iPr** in the crystal are translationally

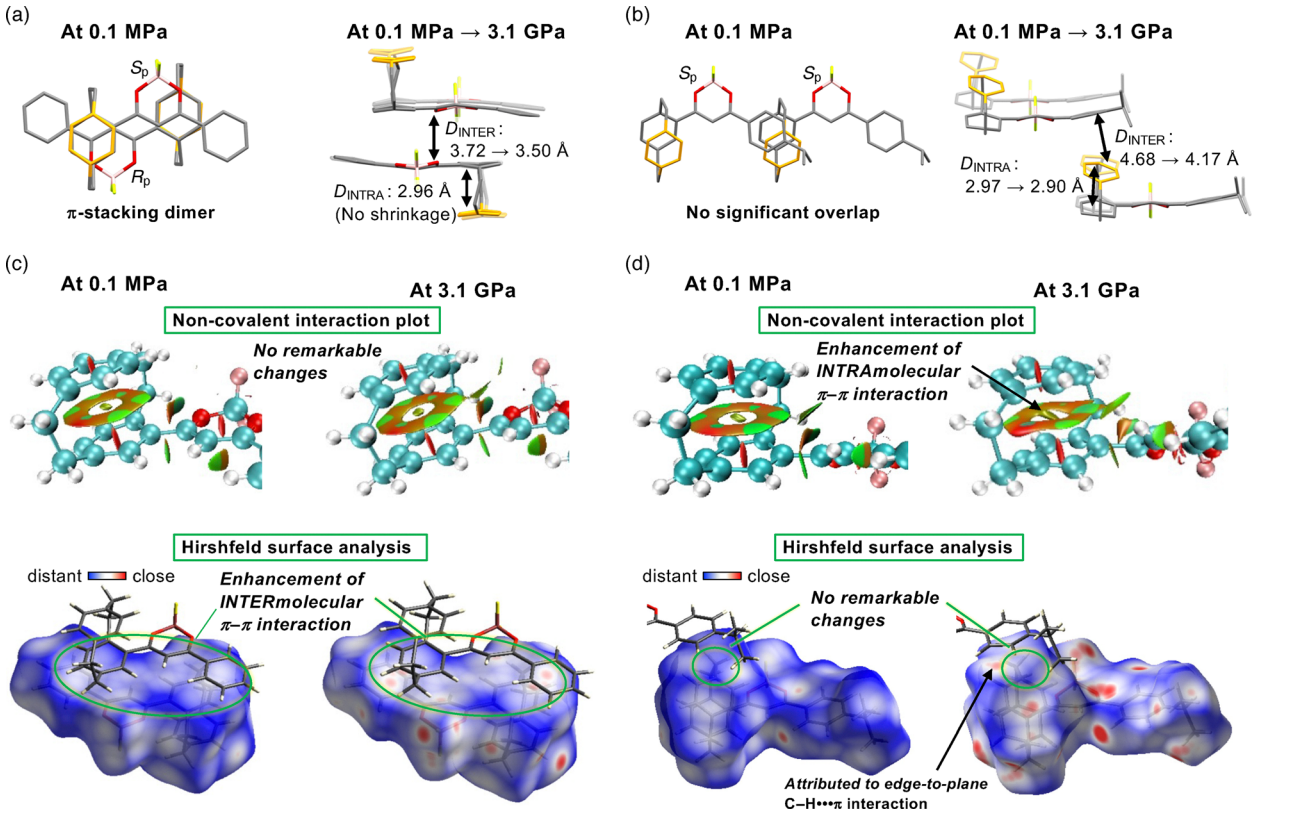

Fig. 4 (a and b) (left) The front views at 0.1 MPa and (right) the side views with overlay of the conformations at 0.1 MPa (shown in translucent) and 3.1 GPa (shown in solid) of the π-stacked dimers of the ***p*CP-H** and ***p*CP-iPr** crystals. (c and d) The visualization of the pressure-induced changes of the (top) intramolecular π–π interactions by the NCI plots and (bottom) intermolecular π–π interactions by the Hirshfeld surface analyses of the ***p*CP-H** and ***p*CP-iPr** crystals. The red-highlighted spots on the Hirshfeld surface show C–H···π and C–H···F interactions.

oriented and have a relationship slipped by 40° with regard to each other. The consequence of this spatial alignment is that the front side of the [2.2]paracyclophane moiety in one molecule faces the back side of the isopropylphenyl moiety in the other molecule (Fig. S6b). Importantly, the intermolecular π–π interaction between molecules in the ***p*CP-iPr** crystal is small owing to the reduced intermolecular overlap between the π-planes. A ***p*CP-iPr** chiral crystal was subjected to X-ray crystallographic analysis at 3.1 GPa. The data show that significant shrinkage of the unit cell occurs (16.4%) and no phase transition takes place (Fig. S8). In accord with the shrinkage, the D_{INTRA} decreases from 2.97 Å at 0.1 MPa to 2.90 Å at 3.1 GPa (Fig. 4b). The NCI plot shows that the interaction region in the [2.2]paracyclophane moiety is expanded (Fig. 4d), suggesting that enhancement of the intramolecular π–π interaction occurs in the ***p*CP-iPr** crystal under high pressure. The pressure increase also promotes a decrease in the distance between ***p*CP-iPr** molecules in the crystal (D_{INTER} from 4.68 Å at 0.1 MPa to 4.17 Å at 3.1 GPa). However, the intermolecular overlap of the π-planes is not large enough to create sufficiently strong intermolecular π–π interactions for it to be the main factor for PFC of the ***p*CP-iPr** crystal. This conclusion suggests that the origin of PFC of the ***p*CP-iPr** crystal is a pressure-induced change in the intramolecular π–π interaction in the [2.2]paracyclophane moiety.

Next, we assessed the pressure-sensitivity of the [2.2]paracyclophane moiety. Pressure-induced changes of the crystal structure of the ***p*CP-iPr** crystal, which showed the simple pressure-sensitivity of the FL over a wide pressure range above 1 GPa, were examined by using density functional theory (DFT) calculations. The results of these calculations, performed using Quantum ESPRESSO ver. 6.3 program package,[47,48] well match the experimentally observed decrease occurring in the unit cell axis length at 3.1 GPa (Fig. S9a). They also indicate that a continuous contraction of the unit cell of the ***p*CP-iPr** crystal occurs in the pressure range of 0.1 MPa to 7.8 GPa and, in fact, the D_{INTRA} value is found to decrease linearly as the pressure increases (Fig. S9b). Although the calculated D_{INTRA} value is about 0.07–0.09 Å larger than the value obtained from X-ray crystallographic analysis, its variations strongly suggest that intramolecular π–π interactions are enhanced by applying pressure at least up to 7.8 GPa and, thus, contribute to PFC of the ***p*CP-iPr** crystal.

Frontier molecular orbitals in *p*CP-H and *p*CP-iPr crystals. DFT calculations using the atomic coordinates derived from the X-ray crystallographic analysis were employed to explore frontier molecular orbitals of the crystals. The HOMO of the monomer in the ***p*CP-H** crystal at 0.1 MPa was found to be mainly localized on the [2.2]paracyclophane moiety (Fig. 5a). On the other hand, the LUMO is delocalized throughout the

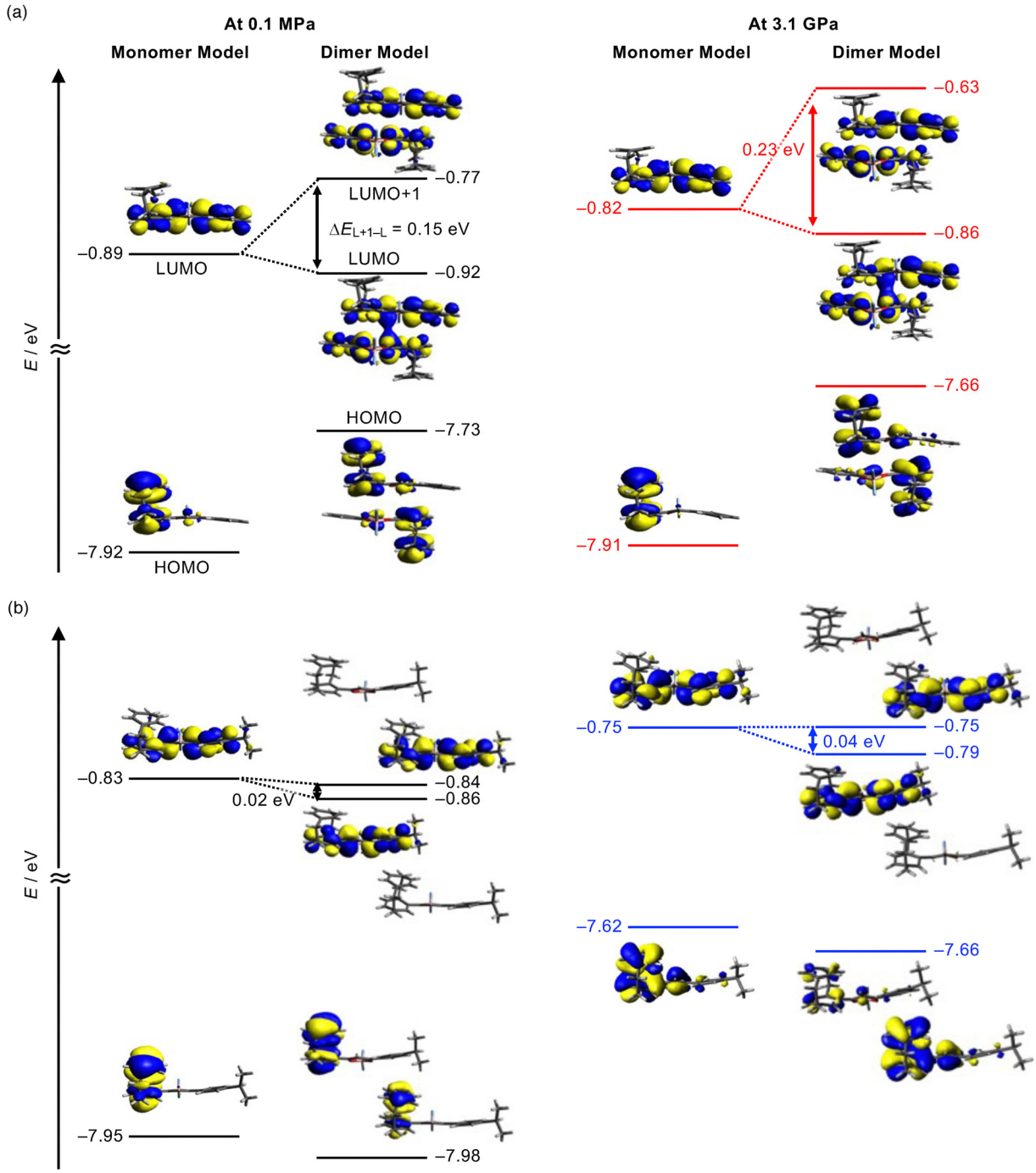

Fig. 5 Energy levels and distributions (isovalue = 0.02) of frontier orbitals of monomers and π-stacked dimers of (a) ***p*CP-H** and (b) ***p*CP-iPr** in crystal. The frontier orbitals are calculated by DFT (ωB97XD/6-31G**) using the molecular coordinates determined by X-ray crystallographic analyses.

entire molecule, except for the overlapping benzene rings of the [2.2]paracyclophane moiety. Energies of the HOMO and LUMO (E_H and E_L) of the monomer in this crystal at 0.1 MPa were calculated to be −7.92 and −0.89 eV, respectively. At 3.1 GPa, the distribution and energies of the HOMO and LUMO of the monomer in the ***p*CP-H** crystal are nearly the same as the values calculated for the crystal at low pressure, which is in accord with the small structural changes found using X-ray crystallographic analysis. Therefore, application of pressure does not impact the electronic states of the monomer in the ***p*CP-H** crystal.

Calculations on the π-stacked dimer in the ***p*CP-H** crystal at 0.1 MPa show that E_H is 0.19 eV larger and E_L is 0.03 eV smaller than those of the monomer, showing a 0.22 eV decrease of HOMO–LUMO transition energy. Because the LUMO and LUMO+1 of the π-stacked dimer have orbital distributions which correspond to a simple combination of those of the monomer LUMOs, the magnitude of the energy difference

between the LUMO and LUMO+1 (ΔE_{L+1-L}) should be a good indicator of the magnitude of the intermolecular π–π interactions. Indeed, ΔE_{L+1-L} is calculated to increase from 0.15 eV at 0.1 MPa to 0.23 eV at 3.1 GPa, indicating that the intermolecular π–π interaction is enhanced under high pressure.

In contrast to those of the monomer in the ***p*CP-H** crystal, the HOMO and LUMO properties of the monomer in the ***p*CP-iPr** crystal display a remarkable response to the applied pressure (Fig. 5b). For example, E_H of the monomer in the ***p*CP-iPr** crystal is −7.95 eV at 0.1 MPa and −7.62 eV at 3.1 GPa, a large increase (0.33 eV) that originates from the enhancement of the intramolecular π–π interactions promoted by the decrease of D_{INTRA}. On the other hand, E_L shows a small increase (0.08 eV) from −0.83 eV at 0.1 MPa to −0.75 eV at 3.1 GPa, because of the lower contribution of the LUMO of the overlapped benzene ring orbitals in the [2.2]paracyclophane moiety. As a result, the HOMO–LUMO transition energy decreases by 0.25 eV.

The calculated frontier molecular orbitals of the π-stacked dimer in the ***p*CP-iPr** crystal are not greatly different from those of the monomer at both 0.1 MPa and 3.1 GPa. This finding indicates that, in contrast to the ***p*CP-H** crystal, the intermolecular π–π interaction in the ***p*CP-iPr** crystal cannot be the key factor for the PFC. This is caused by the weakness of intermolecular orbital interactions, reflected by small ΔE_{L+1-L} values of 0.02 and 0.04 eV resulting from the large (>4 Å) D_{INTER}.

Excited singlet states in *p*CP-H and *p*CP-iPr crystals. To determine the FL domains that contribute to the PFC, time-dependent (TD-) DFT calculations were performed to determine the lowest excited singlet states (E_{S1}) of molecules in the crystals. The results show that E_{S1} of the monomer in the ***p*CP-H** crystal is 3.72 eV at 0.1 MPa and 3.83 eV at 3.1 GPa (Fig. 6a).

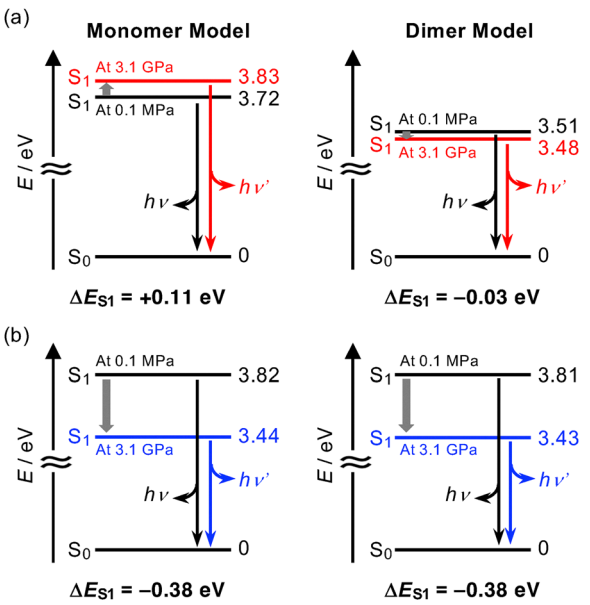

Fig. 6 Relative energy diagrams of the lowest excited singlet states (S_1) and ground states (S_0) of monomers and π-stacked dimers of (a) ***p*CP-H** and (b) ***p*CP-iPr** crystals. ΔE_{S1} refers the changes in E_{S1} promoted by compression.

The 0.11 eV increase of E_{S1} differs from the experimentally observed decrease of $E_{FL,MAX}$, indicating that conformational changes in the monomer cannot be a major factor for the PFC of the ***p*CP-H** crystal. In sharp contrast, E_{S1} of the π-stacked dimer in the ***p*CP-H** crystal was calculated to decrease from 3.51 eV at 0.1 MPa to 3.48 eV at 3.1 GPa. Although a large difference exists between the calculated and observed shifts of $E_{FL,MAX}$ (*ca.* −0.4 eV at 3.3 GPa), the fact that E_{S1} decreases in response to the applied pressure is qualitatively consistent with the PFC. Therefore, the intermolecular π–π interaction is suggested to be a key factor for the "pressure-sensitive" PFC of the ***p*CP-H** crystal.

As indicated by analysis of the frontier molecular orbitals, E_{S1} of the monomer in the ***p*CP-iPr** crystal displays a large decrease from 3.82 eV at 0.1 MPa to 3.44 eV at 3.1 GPa (Fig. 6b), a magnitude (0.38 eV) that is large enough to explain the observed decrease of $E_{FL,MAX}$ (*ca.* −0.2 eV at 3.3 GPa). On the other hand, calculations on the π-stacked dimer in the ***p*CP-iPr** crystal show that E_{S1} has almost the same value as that of the monomer at both 0.1 MPa and 3.1 GPa. This result shows that the pressure sensitivity of the intermolecular π–π interaction in the ***p*CP-iPr** crystal only slightly influences PFC, suggesting that the enhancement of the intramolecular π–π interaction in the [2.2]paracyclophane moiety is the main contributor to the "pressure-insensitive" PFC of the ***p*CP-iPr** crystal.

Conclusions

In this study, we demonstrated that a correlation exists between the PFC properties and crystal structures of ***p*CP-H** and ***p*CP-iPr**. Both the ***p*CP-H** and ***p*CP-iPr** crystals display remarkable PFC, reflected in a redshift greater than 100 nm under high pressure applied by using the DAC. However, the pressure sensitivity and mechanisms of PFC of these crystals differ. The PFC of the ***p*CP-H** crystal has about a two-fold higher pressure sensitivity than that of the ***p*CP-iPr** crystal. X-ray crystallographic analyses show that ***p*CP-H** forms a π-stacked dimer possessing a remarkably large intermolecular π–π interaction. The results of X-ray crystallographic analysis under high pressure and (TD-) DFT calculations show that PFC of the ***p*CP-H** crystal originates from an enhancement of intermolecular π–π interactions promoted by an increase in applied pressure. On the other hand, the ***p*CP-iPr** crystal does not form a π-stacked dimer like the ***p*CP-H** crystal does. Therefore, intermolecular π–π interactions in this crystal are weak even under high pressure. In contrast, the ***p*CP-iPr** crystal displays an enhancement of intramolecular π–π interactions caused by shrinkage of the [2.2]paracyclophane moiety under high pressure, which is suggested to be the major factor of the PFC of the ***p*CP-iPr** crystal.

The results of this investigation demonstrate that alterations in intramolecular π–π interactions in the [2.2]paracyclophane moiety can play a novel role in the design of new pressure sensors. Our findings suggest that PFC caused by the presence of the [2.2]paracyclophane moiety would be significantly useful because it would convey high linearity over a wide range of applied pressures. It is also noteworthy that the pressure

sensitivity of the [2.2]paracyclophane moiety should not be influenced by the presence of other molecular moieties, and thus, it should be possible to control the characteristics of the PFC by introducing the [2.2]paracyclophane moiety into a wide variety of luminophores. Therefore, it should be possible to incorporate the [2.2]paracyclophane moiety in the design of pressure-sensitive materials. In contrast to initial expectations, this study also revealed that the pressure sensitivity of the [2.2]paracyclophane moiety strongly depends on the structure of the crystal, especially on chirality in the three-dimensionally asymmetric [2.2]paracyclophane moiety. The results obtained from this study have provided valuable insight into not only the mechanism of PFC of crystalline organic substances but also the structural and electronic properties of the [2.2]paracyclophane ring system.

Experimental section

General

Melting points (mp) were measured using a Yanaco MP-500 apparatus and are reported uncorrected. ^{1}H and ^{13}C NMR spectra were recorded on a Bruker AVANCE NEO 400 spectrometer, operating at 400 and 100 MHz for ^{1}H and ^{13}C NMR, respectively. Chemical shifts (δ_{ppm}) were reported in ppm with respect to tetramethylsilane (TMS, 0.00 ppm in ^{1}H NMR) and $CDCl_3$ (77.0 ppm in ^{13}C NMR) as the internal standard. Atmospheric pressure solids analysis probe (ASAP) mass spectroscopy (MS) was carried out using a Shimadzu LCMS-2020 and LabSolutions LCMS software. Fourier transform infrared (FT-IR) spectra were recorded on a JASCO FT/IR-8300 spectrophotometer with the attenuated total reflection (ATR) method. Elemental analyses were performed at the Advanced Science Research Center at Kanazawa University or the Analytical Center, Graduate School of Science, Osaka Metropolitan University. UV-vis absorption spectra were recorded on a JASCO V-570 spectrophotometer. FL spectra at ambient pressure were recorded on a JASCO FP-8500 spectrophotometer. τ_{FL} values were determined using a HORIBA Jobin Yvon FluoroCube lifetime spectrofluorometer equipped with a HORIBA NanoLED-370 (excitation wavelength, λ_{EX} = 370 nm) as an excitation light source and analyzed using DAS6 FL decay analysis software. Φ_{FL} values were recorded on a Hamamatsu Photonics C9920-02 absolute photoluminescence quantum yield measurement system using the integrating sphere method.

Preparation of organic substances

Dry tetrahydrofuran (THF) was prepared by using a Glass-Contour solvent dispensing system. Dry toluene was purified by pre-drying over CaH_2 and distillation from Na. Solvents of spectroscopic grade were used for spectroscopic analyses.

Synthetic procedures

Synthesis of 1-(4-isopropylphenyl)-3-(4-[2.2]paracyclophanyl)propane-1,3-dione (3-iPr). To a suspension of NaH (60% dispersion in mineral oil, 1.59 g, 40.0 mmol) in THF (50 mL) was added 4-acetyl[2.2]paracyclophane (**1**, 2.50 g, 10.00 mmol) at room temperature under an argon atmosphere. To this mixture, a solution of 4-isopropylbenzoate (**2-iPr**, 2.67 g, 15.0 mmol) in THF (25 mL) was added dropwise (1–2 drops per s). The mixture was stirred at reflux for 18 h and then cooled to room temperature. After quenching by adding 10% aqueous HCl (250 mL), the aqueous layer was extracted with ethyl acetate (80 mL × 3). The combined organic layers were washed with brine (150 mL), dried over anhydrous Na_2SO_4 and filtered. The filtrate was concentrated by evaporation under reduced pressure. Purification of the crude material by silica-gel column chromatography (ethyl acetate/*n*-hexane = 1/19) followed by recrystallization from ethyl acetate afforded pure **3-iPr** as pale orange blocks (2.00 g, 5.03 mmol) in a 50% yield. The corresponding 1,3-diketo-tautomer was not observed by ^{1}H NMR analysis in $CDCl_3$. **3-iPr**: pale orange blocks; mp 103–104 °C (ethyl acetate); ^{1}H NMR ($CDCl_3$, 400 MHz) δ_{ppm} 1.29 (d, J = 6.9 Hz, 6H), 2.92–3.22 (m, 1H + 7H), 3.91 (m, 1H), 6.45–6.47 (m, 2H), 6.54–6.68 (m, 5H), 6.91 (d, J = 1.8 Hz, 1H), 7.34 (AA′XX′, J = 8.3 Hz, 2H), 7.90 (AA′XX′, J = 8.3 Hz, 2H), 16.87 (s, 1H); ^{13}C NMR ($CDCl_3$, 100 MHz) δ_{ppm} 23.7 (2C), 34.2, 35.2, 35.3, 35.5, 35.7, 96.5, 126.8 (2C), 127.2 (2C), 131.7, 132.4, 132.5, 132.6, 132.7, 133.2, 135.8, 136.4, 136.9, 139.3, 139.8, 140.0, 140.3, 153.8, 184.3, 189.0; IR (ATR, neat) ν/cm^{-1} 2963, 2928, 1608, 1593 (C═O), 1547, 1505, 1448, 1301, 1284, 1228, 1190, 1043, 901, 859, 851, 829, 800, 716, 707, 664; MS (ASAP) m/z 397 ([M + H]$^+$); Anal. Calcd for $C_{28}H_{28}O_2$: C, 84.81; H, 7.12; N, 0.00. Found: C, 84.87; H, 7.10; N, 0.00.

Synthesis of 1-(4-isopropylphenyl)-3-(4-[2.2]paracyclopha-nyl)-propane-1,3-dionatoboron difluoride (*p*CP-iPr). To a solution of **3-iPr** (1.19 g, 3.00 mmol) in toluene (66 mL) was added a boron trifluoride–diethyl ether complex (0.57 mL, 4.5 mmol) under an argon atmosphere. After the mixture was stirred at room temperature for 12 h, volatile materials were removed under reduced pressure. Recrystallization of the crude material from ethyl acetate afforded pure ***p*CP-iPr** (0.667 g, 1.50 mmol) as yellow powder in a 50% yield. ***p*CP-iPr**: yellow powder; mp 181–182 °C (ethyl acetate); ^{1}H NMR ($CDCl_3$, 400 MHz) δ_{ppm} 1.30 (d, J = 6.9 Hz, 6H), 2.98–3.24 (m, 1H + 7H), 3.98 (m, 1H), 6.47 (dd, J = 7.7, 1.6 Hz, 1H), 6.54–6.66 (m, 4H), 6.77 (dd, J = 7.8, 1.8 Hz, 1H), 6.81 (s, 1H), 7.08 (d, J = 1.8 Hz, 1H), 7.41 (AA′XX′, J = 8.4 Hz, 2H), 8.06 (AA′XX′, J = 8.4 Hz, 2H); ^{13}C NMR ($CDCl_3$, 100 MHz) δ_{ppm} 23.5 (2C), 34.5, 35.0, 35.1, 35.6, 36.6, 96.3, 127.3 (2C), 129.1 (2C), 129.7, 132.1, 132.2, 132.7, 132.8, 132.2, 134.1, 137.2, 138.3, 139.2, 139.7, 140.7, 143.1, 157.3, 181.9, 185.0; IR (ATR, neat) ν/cm^{-1} 2965, 2935, 1604, 1537, 1519, 1499, 1474, 1457, 1427, 1374, 1362, 1306, 1286, 1250, 1188, 1159, 1146, 1120, 1095, 1071, 1056, 1038, 1011, 976, 863, 823, 811, 797, 719, 698, 678, 669; MS (ASAP) m/z 445 ([M + H]$^+$); Anal. Calcd for $C_{28}H_{27}BF_2O_2$: C, 75.69; H, 6.13; N, 0.00. Found: C, 75.35; H, 6.45; N, 0.16.

FL measurement of crystals under high pressure

FL spectra of crystals under high pressure were recorded on a Hamamatsu Photonics PMA-11 spectrophotometer with a Panasonic UJ-30 UV-LED system as an excitation light source (λ_{EX} = 365 nm). Crystals were placed in a hole (diameter: 300 μm) of

an SUS301 steel gasket equipped with DAC for applying isotropic pressure. Kerosene was used as a pressure-transmitting medium.[17,35,49] Hydrocarbons, including petroleum ether and kerosene, have been known to maintain good hydrostaticity up to 10 GPa.[50] The applied pressure was determined by using the ruby FL method.[51] Photographs of crystals in DAC were taken on a FL microscope using irradiation by a 365-nm UV light or white LED light.

X-ray crystallographic analysis

General. Single crystals for X-ray crystallographic analyses were obtained by slow vapor diffusion of *n*-hexane into toluene solution for ***p*CP-H** or ethyl acetate solution for ***p*CP-iPr**. The X-ray diffraction data were collected at 293 K on a Rigaku XtaLAB Synergy-DW diffractometer with a Rigaku HyPix-6000 area detector by using Mo Kα radiation (λ = 0.71075 Å). The high-pressure measurements were performed using a sample holder equipped with the DAC and kerosene as the pressure medium. The inner pressure in the DAC was determined using the unit-cell parameters of NaCl.[52] The structures were resolved by using the intrinsic phasing method and a SHELXT program[53] and were refined by using the least squares method of the squared amplitudes of the structure factor using the SHELXL program.[54] For treatment of the ambient-pressure measurement data, non-hydrogen atoms were refined using an anisotropic temperature factor, while for the high-pressure measurement data, non-hydrogen atoms were refined using an isotropic temperature factor because of the limited opening angle of the DAC. The hydrogen atoms for both ambient- and high-pressure measurement data were fixed at the positions calculated by the riding model. The Olex2 Version 1.3 program[55] was used for all analyses.

Crystal data for *p*CP-H at 0.1 MPa. Yellow block, trigonal, $R\bar{3}$, $a = b$ = 27.579(4) Å, c = 13.7469(15) Å, V = 9055(3) Å^3, Z = 18, ρ_{calcd} = 1.328 g cm^{-3}, T = 293 K, $2\theta_{max}$ = 57.31°, 10 588 reflections measured, 4745 unique reflections, R_{int} = 0.0652, 271 parameters, R_1 = 0.0765 ($I > 2\sigma(I)$), wR_2 = 0.2433 (all data), CCDC-2241676.

Crystal data for *p*CP-H at 3.1 GPa. Yellow block, trigonal, $R\bar{3}$, $a = b$ = 26.750(4) Å, c = 13.298(17) Å, V = 8241(11) Å^3, Z = 18, ρ_{calcd} = 1.573 g cm^{-3}, T = 293 K, $2\theta_{max}$ = 50.696°, 5626 reflections measured, 1603 unique reflections, R_{int} = 0.0913, 271 parameters, R_1 = 0.1341 ($I > 2\sigma(I)$), wR_2 = 0.4339 (all data), CCDC-2241677.

Crystal data for *p*CP-iPr at 0.1 MPa. Yellow block, orthorhombic, $P2_12_12_1$, a = 10.7074(6) Å, b = 14.6344(8) Å, c = 14.8516(8) Å, V = 2327.2(2) Å^3, Z = 4, ρ_{calcd} = 1.268 g cm^{-3}, T = 293 K, $2\theta_{max}$ = 74.866°, 15 966 reflections measured, 4754 unique reflections, R_{int} = 0.0289, 300 parameters, R_1 = 0.0435 ($I > 2\sigma(I)$), wR_2 = 0.1182 (all data), CCDC-2241678.

Crystal data for *p*CP-iPr at 3.1 GPa. Yellow block, orthorhombic, $P2_12_12_1$, a = 9.9470(13) Å, b = 14.3749(17) Å, c = 13.61(4) Å, V = 1946(6) Å^3, Z = 4, ρ_{calcd} = 1.517 g cm^{-3}, T = 293 K, $2\theta_{max}$ = 41.594°, 6130 reflections measured, 523 unique reflections, R_{int} = 0.0843, 133 parameters, R_1 = 0.0820 ($I > 2\sigma(I)$), wR_2 = 0.2184 (all data), CCDC-2241679.

Computational methods

Molecular orbital distributions and energies of singlet states in crystals were calculated by using DFT or TD-DFT with the ωB97XD functional and the 6-31G** basis set using the Gaussian 09W program.[56] The crystal coordinates derived from the X-ray crystallographic analyses were used for these calculations without geometry optimization. The non-covalent interaction plots were analysed using the Multiwfn program[57–59] and visualized using the VMD v1.9.3 program.[60] The Hirshfeld surface analyses were conducted using the CrystalExplorer v17.5 program.[61] The geometry optimizations of the crystal structures under high pressure were carried out by using the PWSCF program in the Quantum ESPRESSO ver. 6.3 program package[47,48] with the van der Waals density functional (vdW-DF) for the non-local correlation.[62,63] The projector augmented wave (PAW) method was employed to describe the inner-shell electrons of each atom as pseudopotentials with respect to the valence electrons. The energy cut-off for the plane wave basis set and the charge density were 49 and 325 Ry, respectively. Convergence tolerance for the self-consistent field (SCF) calculation was set to the estimated total energy error of less than 1.0×10^{-6} Ry. For the structural optimization, the convergence tolerance of the total energy, the force, and the pressure on the unit cell were set to 1.0×10^{-4} a.u., 1.0×10^{-3} a.u., and 0.05 GPa, respectively.

Author contributions

T. Ogaki and H. Ikeda designed this research project. S. Irii, T. Ogaki, and Y. Matsui analysed the experimental data. S. Irii and S. Yamamoto synthesized molecules. S. Irii measured photophysical properties under ambient pressure. H. Miyashita, K. Nobori, and H. Iida carried out the high-pressure FL measurements under the supervision of Y. Ozawa and M. Abe. H. Sato carried out the X-ray crystallographic analyses under ambient and high pressures. S. Irii conducted the theoretical calculations. The manuscript was prepared by contribution of all authors. All authors approved the final version of the manuscript.

Conflicts of interest

There are no conflicts to declare.

Data availability

The data supporting this article have been included as part of the supplementary information (SI). Supplementary information: ^{1}H and ^{13}C NMR spectra, photophysical data, crystal structures, and DFT calculation results. See DOI: **https://doi.org/10.1039/d5tc03195h**.

CCDC 2241676–2241679 contain the supplementary crystallographic data for this paper.[64a–d]

Acknowledgements

This study was partially supported by JSPS KAKENHI Grants (no. JP24H01092, JP22K14667, JP22H05377, JP20K15264, JP21H04564, JP22K05069, JP22K05147, JP16H06514, JP21K19029, JP17H06375, JP17H06371, JP18H01967, and JP21H05494); by grants from the Konica Minolta Science and Technology Foundation, Tobe Maki Foundation (25-JA-016), the Hattori Hokokai Foundation, Mayekawa Houonkai Foundation (A3-24006), and the 2024 Osaka Metropolitan University Strategic Research Promotion Project (Young Researcher); and by JST Grants of the establishment of university fellowships towards the creation of science technology innovation (no. JPMJFS2138) and of SPRING (no. JPMJSP2139).

References

1 S. Saha, M. K. Mishra, C. M. Reddy and G. R. Desiraju, *Acc. Chem. Res.*, 2018, **51**, 2957–2967.
2 M. Kato, H. Ito, M. Hasegawa and K. Ishii, *Chem. – Eur. J.*, 2019, **25**, 5105–5112.
3 A. Li, S. Xu, C. Bi, Y. Geng, H. Cui and W. Xu, *Mater. Chem. Front.*, 2021, **5**, 2588–2606.
4 L. Wang, K. Q. Ye and H. Y. Zhang, *Chin. Chem. Lett.*, 2016, **27**, 1367–1375.
5 C. Li, C. Lv, M. Ouyang and Y. Zhang, *ChemPhysChem*, 2023, **24**, e202200922.
6 D. J. Mitchell, G. B. Schuster and H. G. Drickamer, *J. Am. Chem. Soc.*, 1977, **99**, 1145–1148.
7 R. T. Roginski, J. R. Shapley and H. G. Drickamer, *J. Phys. Chem.*, 1988, **92**, 4316–4319.
8 Z. A. Dreger, J. M. Lang and H. G. Drickamer, *Chem. Phys.*, 1993, **169**, 361–368.
9 J. M. Lang, Z. A. Dreger and H. G. Drickamer, *J. Phys. Chem.*, 1994, **98**, 11308–11315.
10 A. Jayaraman, *Rev. Mod. Phys.*, 1983, **55**, 65–108.
11 H.-K. Mao, X.-J. Chen, Y. Ding, B. Li and L. Wang, *Rev. Mod. Phys.*, 2018, **90**, 015007.
12 V. Schettino and R. Bini, *Chem. Soc. Rev.*, 2007, **36**, 869.
13 G. J. Piermarini, A. D. Mighell, C. E. Weir and S. Block, *Science*, 1969, **165**, 1250–1255.
14 M. M. Thiéry and J. M. Léger, *J. Chem. Phys.*, 1988, **89**, 4255–4271.
15 K. Nagura, S. Saito, H. Yusa, H. Yamawaki, H. Fujihisa, H. Sato, Y. Shimoikeda and S. Yamaguchi, *J. Am. Chem. Soc.*, 2013, **135**, 10322–10325.
16 S. Mosca, A. Milani, M. Peña-Álvarez, S. Yamaguchi, V. Hernández, M. C. Ruiz Delgado and C. Castiglioni, *J. Phys. Chem. C*, 2018, **122**, 17537–17543.
17 T. Ono, Y. Tsukiyama, A. Taema, H. Sato, H. Kiyooka, Y. Yamaguchi, A. Nagahashi, M. Nishiyama, Y. Akahama, Y. Ozawa, M. Abe and Y. Hisaeda, *ChemPhotoChem*, 2018, **2**, 416–420.
18 Y. Dai, H. Liu, T. Geng, F. Ke, S. Niu, K. Wang, Y. Qi, B. Zou, B. Yang, W. L. Mao and Y. Lin, *J. Mater. Chem. C*, 2021, **9**, 934–938.
19 S. Hu, Z. Yao, X. Ma, L. Yue, L. Chen, R. Liu, P. Wang, H. Li, S.-T. Zhang, D. Yao, T. Cui, B. Zou and G. Zou, *J. Phys. Chem. Lett.*, 2022, 1290–1299.
20 X. Wang, Q. Liu, H. Yan, Z. Liu, M. Yao, Q. Zhang, S. Gong and W. He, *Chem. Commun.*, 2015, **51**, 7497–7500.
21 X. Cao, W. Wang, J. Peng, A. Li, Q. Li, W. Xu and S. Xu, *Cryst. Growth Des.*, 2024, **24**, 8822–8828.
22 Q. Wang, N. Sui, X. Gao, X. Chi, L. Pan, R. Lu, H. Zhang, Z. Kang, B. Zhao and Y. Wang, *J. Phys. Chem. B*, 2021, **125**, 4132–4140.
23 S. Yang, Z. Feng, Z. Fu, K. Zhang, S. Chen, Y. Yu, B. Zou, K. Wang, L. Liao and Z. Jiang, *Angew. Chem., Int. Ed.*, 2022, **61**, e202206861.
24 M. Wu, H. Liu, H. Liu, T. Lu, S. Wang, G. Niu, L. Sui, F. Bai, B. Yang, K. Wang, X. Yang and B. Zou, *J. Phys. Chem. Lett.*, 2022, **13**, 2493–2499.
25 X. Wang, C. Qi, Z. Fu, H. Zhang, J. Wang, H.-T. Feng, K. Wang, B. Zou, J. W. Y. Lam and B. Z. Tang, *Mater. Horiz.*, 2021, **8**, 630–638.
26 A. Li, J. Wang, C. Bi, Z. Chen, S. Xu, K. Wang, J. Wang and Z. Li, *J. Mater. Chem. C*, 2024, **12**, 17377–17385.
27 C. J. Brown and A. C. Farthing, *Nature*, 1949, **164**, 915–916.
28 D. Cram and H. Steinberg, *J. Am. Chem. Soc.*, 1951, **73**, 5691–5704.
29 H. Wolf, D. Leusser, M. R. V. Jørgensen, R. Herbst-Irmer, Y.-S. Chen, E.-W. Scheidt, W. Scherer, B. B. Iversen and D. Stalke, *Chem. – Eur. J.*, 2014, **20**, 7048–7053.
30 E. Elacqua and L. R. MacGillivray, *Eur. J. Org. Chem.*, 2010, 6883–6894.
31 G. C. Bazan, *J. Org. Chem.*, 2007, **72**, 8615–8635.
32 T. Sato, K. Torizuka, M. Shimizu, Y. Kurihara and N. Yoda, *Bull. Chem. Soc. Jpn.*, 1979, **52**, 2420–2423.
33 T. Miyazaki, M. Shibahara, J. I. Fujishige, M. Watanabe, K. Goto and T. Shinmyozu, *J. Org. Chem.*, 2014, **79**, 11440–11453.
34 W. Li, Z. Sui, H. Liu, Z. Zhang and H. Liu, *J. Phys. Chem. C*, 2014, **118**, 16028–16034.
35 S. Irii, T. Ogaki, H. Miyashita, K. Nobori, Y. Ozawa, M. Abe, H. Sato, E. Ohta, Y. Matsui and H. Ikeda, *Tetrahedron Lett.*, 2022, **101**, 153913.
36 G. T. Morgan and R. B. Tunstall, *J. Chem. Soc., Trans.*, 1924, **125**, 1963–1967.
37 A. G. Mirochnik, E. V. Gukhman, V. E. Karasev and P. A. Zhikhareva, *Russ. Chem. Bull.*, 2000, **49**, 1024–1027.
38 A. G. Mirochnik, B. V. Bukvetskii, E. V. Gukhman, P. A. Zhikhareva and V. E. Karasev, *Russ. Chem. Bull.*, 2001, **50**, 1612–1615.
39 M. Tanaka, S. Muraoka, Y. Matsui, E. Ohta, A. Sakai, T. Ogaki, Y. Yoshimoto, K. Mizuno and H. Ikeda, *ChemPhotoChem*, 2017, **1**, 188–197.
40 M. Tanaka, S. Muraoka, Y. Matsui, E. Ohta, T. Ogaki, K. Mizuno and H. Ikeda, *Photochem. Photobiol. Sci.*, 2017, **16**, 845–853.
41 S. Galembeck, R. Orenha, R. Madeira, L. Peixoto and R. Parreira, *J. Braz. Chem. Soc.*, 2021, **32**, 1447–1455.
42 I. Østrøm, A. O. Ortolan, F. S. S. Schneider, G. F. Caramori and R. L. T. Parreira, *J. Org. Chem.*, 2018, **83**, 5114–5122.

43 C. L. Firme and D. M. Araújo, *Comput. Theor. Chem.*, 2018, **1135**, 18–27.
44 J. J. McKinnon, D. Jayatilaka and M. A. Spackman, *Chem. Commun.*, 2007, 3814–3816.
45 M. A. Spackman and D. Jayatilaka, *CrystEngComm*, 2009, **11**, 19–32.
46 J. J. McKinnon, M. A. Spackman and A. S. Mitchell, *Acta Crystallogr., Sect. B: Struct. Sci.*, 2004, **60**, 627–668.
47 P. Giannozzi, S. Baroni, N. Bonini, M. Calandra, R. Car, C. Cavazzoni, D. Ceresoli, G. L. Chiarotti, M. Cococcioni, I. Dabo, A. Dal Corso, S. de Gironcoli, S. Fabris, G. Fratesi, R. Gebauer, U. Gerstmann, C. Gougoussis, A. Kokalj, M. Lazzeri, L. Martin-Samos, N. Marzari, F. Mauri, R. Mazzarello, S. Paolini, A. Pasquarello, L. Paulatto, C. Sbraccia, S. Scandolo, G. Sclauzero, A. P. Seitsonen, A. Smogunov, P. Umari and R. M. Wentzcovitch, *J. Phys.: Condens. Matter*, 2009, **21**, 395502.
48 P. Giannozzi, O. Andreussi, T. Brumme, O. Bunau, M. Buongiorno Nardelli, M. Calandra, R. Car, C. Cavazzoni, D. Ceresoli, M. Cococcioni, N. Colonna, I. Carnimeo, A. Dal Corso, S. de Gironcoli, P. Delugas, R. A. DiStasio, A. Ferretti, A. Floris, G. Fratesi, G. Fugallo, R. Gebauer, U. Gerstmann, F. Giustino, T. Gorni, J. Jia, M. Kawamura, H.-Y. Ko, A. Kokalj, E. Küçükbenli, M. Lazzeri, M. Marsili, N. Marzari, F. Mauri, N. L. Nguyen, H.-V. Nguyen, A. Otero-de-la-Roza, L. Paulatto, S. Poncé, D. Rocca, R. Sabatini, B. Santra, M. Schlipf, A. P. Seitsonen, A. Smogunov, I. Timrov, T. Thonhauser, P. Umari, N. Vast, X. Wu and S. Baroni, *J. Phys.: Condens. Matter*, 2017, **29**, 465901.
49 M. K. Tran, J. Levallois, A. Akrap, J. Teyssier, A. B. Kuzmenko, F. Lévy-Bertrand, R. Tediosi, M. Brandt, P. Lerch and D. van der Marel, *Rev. Sci. Instrum.*, 2015, **86**, 105102.
50 N. Tateiwa and Y. Haga, *Rev. Sci. Instrum.*, 2009, **80**, 123901.
51 G. J. Piermarini, S. Block, J. D. Barnett and R. A. Forman, *J. Appl. Phys.*, 1975, **46**, 2774–2780.
52 D. L. Decker, *J. Appl. Phys.*, 1971, **42**, 3239–3244.
53 G. M. Sheldrick, *Acta Crystallogr. Sect. A Found. Adv.*, 2015, **71**, 3–8.
54 G. M. Sheldrick, *Acta Crystallogr. Sect. C Struct. Chem.*, 2015, **71**, 3–8.
55 O. V. Dolomanov, L. J. Bourhis, R. J. Gildea, J. A. K. Howard and H. Puschmann, *J. Appl. Crystallogr.*, 2009, **42**, 339–341.
56 M. J. Frisch, G. W. Trucks, H. B. Schlegel, G. E. Scuseria, M. A. Robb, J. R. Cheeseman, G. Scalmani, V. Barone, G. A. Petersson, X. L. H. Nakatsuji, M. Caricato, A. Marenich, J. Bloino, B. G. Janesko, R. Gomperts, B. Mennucci, H. P. Hratchian, J. V. Ortiz, A. F. Izmaylov, J. L. Sonnenberg, D. Williams-Young, F. Ding, F. Lipparini, F. Egidi, J. Goings, B. Peng, A. Petrone, T. Henderson, D. Ranasinghe, V. G. Zakrzewski, N. R. J. Gao, G. Zheng, W. Liang, M. Hada, M. Ehara, K. Toyota, R. Fukuda, J. Hasegawa, M. Ishida, T. Nakajima, Y. Honda, O. Kitao, H. Nakai, T. Vreven, K. Throssell, J. A. Montgomery, J. E. P. Jr., F. Ogliaro, M. Bearpark, J. J. Heyd, E. Brothers, K. N. Kudin, V. N. Staroverov, T. Keith, R. Kobayashi, J. Normand, K. Raghavachari, A. Rendell, J. C. Burant, S. S. Iyengar, J. Tomasi, M. Cossi, J. M. Millam, M. Klene, C. Adamo, R. Cammi, J. W. Ochterski, R. L. Martin, K. Morokuma, O. Farkas, J. B. Foresman and D. J. Fox, *Gaussian 09*.
57 T. Lu and F. Chen, *J. Comput. Chem.*, 2012, **33**, 580–592.
58 T. Lu, *J. Chem. Phys.*, 2024, **161**, 082503.
59 T. Lu and Q. Chen, *Chem. Methods*, 2021, **1**, 231–239.
60 W. Humphrey, A. Dalke and K. Schulten, *J. Mol. Graph.*, 1996, **14**, 33–38.
61 P. R. Spackman, M. J. Turner, J. J. McKinnon, S. K. Wolff, D. J. Grimwood, D. Jayatilaka and M. A. Spackman, *J. Appl. Crystallogr.*, 2021, **54**, 1006–1011.
62 H. Rydberg, M. Dion, N. Jacobson, E. Schröder, P. Hyldgaard, S. I. Simak, D. C. Langreth and B. I. Lundqvist, *Phys. Rev. Lett.*, 2003, **91**, 126402.
63 M. Dion, H. Rydberg, E. Schröder, D. C. Langreth and B. I. Lundqvist, *Phys. Rev. Lett.*, 2004, **92**, 246401.
64 (*a*) CCDC 2241676: Experimental Crystal Structure Determination, 2025, DOI: **10.5517/ccdc.csd.cc2f7n4h**; (*b*) CCDC 2241677: Experimental Crystal Structure Determination, 2025, DOI: **10.5517/ccdc.csd.cc2f7n5j**; (*c*) CCDC 2241678: Experimental Crystal Structure Determination, 2025, DOI: **10.5517/ccdc.csd.cc2f7n6k**; (*d*) CCDC 2241679: Experimental Crystal Structure Determination, 2025, DOI: **10.5517/ccdc.csd.cc2f7n7l**.

